Electronic Supplementary Information (ESI)

Electrochemically customized assembly of hybrid xerogel material *via* combined covalent and non-covalent conjugation chemistry: An approach for boosting the cycling performance of pseudocapacitors

Taniya Purkait, Dimple, Navpreet Kamboj, Manisha Das, Subhajit Sarkar, Abir De Sarkar, and Ramendra Sundar Dey*

Institute of Nano Science and Technology (INST), Mohali-160064, Punjab, India.

Email: rsdey@inst.ac.in

Materials

Highly pure graphite flakes (<20μm), phosphorous pentoxide (P_2O_5, >98%), potassium permanganate ($KMnO_4$), Dopamine HCl, Tetraethylammonium tetrafluoroborate (Et_4NBF_4), ethylene carbonate (EC) and, diethyl carbonate (DEC) were purchased from Sigma Aldrich and were used as received. Sulphuric acid (H_2SO_4) and, hydrochloric acid (HCl) were purchased from Merck chemicals India. Poly (vinyl) alcohol (M.W. 89000-98000) was purchased from Alfa Aesar (Thermo Fischer Scientific Chemicals Inc.; US). PET sheets (d = 0.3 mm) were purchased from local market. Before use, all the PET sheets were washed with de-ionised (DI) water. All other chemicals used were at least of analytical grade and were used without any further purification. All aqueous solution was prepared using Millipore water.

Characterization Details

Electrochemical measurements like cyclic voltammetry, galvanostatic charge-discharge, Electrochemical Impedance Spectroscopy (EIS), etc. were performed on a CHI 760E electrochemical workstation. A platinum wire was assigned as a counter electrode while all calculations were made against the Ag/AgCl (3 M) electrode that was selected as the reference. The electrical conductivity of the hybrid material was measured by a two-probe method using a Keithley 2635B source meter.

The surface morphological characterization along with determination of elemental composition of the xerogel morphology were investigated using Scanning Electron Microscopy (SEM Jeol JSMIT300) equipped with a Bruker XFlash 6130 Energy Dispersive X-ray Spectroscopy (EDS). Transmission Electron Microscopy (TEM) studies were carried out on a JEM2100 instrument suitable for High-Resolution TEM (HRTEM) studies. Atomic force microscopy (AFM, Bruker Multimode 8) was used to investigate the surface topologies of the synthesized active material. X-ray Diffraction (XRD) spectroscopic study was carried

out on a Bruker D8 Advances instrument using Cu-Kα (λ = 1.5406 Å) radiation in the 2θ range from 5° to 70° with an acceleration voltage of 40 KV. Fourier transform Infrared (FTIR) spectroscopy was carried out on an Agilent technology Cary 600 series FTIR instrument at room temperature. For FTIR analysis, all the samples were mixed with KBr and then finely ground to make a pellet. X-Ray photoelectron (XPS) spectroscopy was performed on a KAlpha plus XPS system by ThermoFisher Scientific instruments in an ultrahigh vacuum chamber ($7X10^{-9}$ torr) using Al-K_α radiation (1486.6 eV). Raman Spectroscopy was performed on a WITEC Focus Innovations Alpha-300 Raman confocal microscope at a laser wavelength of 532 nm. Nitrogen adsorption-desorption analysis was done at 77 K on an Autosorb iQ2 instrumental setup to examine the surface area by Brunauer Emmett Teller (BET) method. The samples were degassed at 150 °C for more than 12 h under vacuum conditions. The pore size distribution was computed by the Barrett-Joyner-Halenda pore size distribution (BJH) technique.

First-principle calculations were performed based on density functional theory (DFT) as implemented in Vienna Ab-initio Simulation Package (VASP) for the composed systems (DA-rGO). Projected augmented wave (PAW) and the exchange-correlation energy was described at the level of Perdew-Burke-Ernzerhof (PBE) variant of generalized gradient approximation (GGA). A plane wave cut-off of 400 eV was used. The structure optimization was carried out by relaxing the forces on all the atoms until 0.01 eV/A force tolerance was achieved. The Brillouin zone was sampled with 5×5×1 Monkhorst mesh-sampling during structure relaxations. Gaussian smearing was used to determine how the partial occupancies are set for each wave function.

To model the DA-rGO system, we considered the composite of DA adsorbed on graphene in different orientations, namely parallel (P_1 or P_2) or vertical (V_1, V_2 or V_3) to the surface of graphene. Here P_1 is a stacked site and P_2 is a hollow site. We use a

7×7×1 periodic supercell of graphene for our calculations and set the translation vector along the z direction as 25 Å with sufficient vacuum to ensure that no interaction occurs between the adjacent molecules. The structure drawing and charge density visualization were generated using VESTA.

Synthesis of graphene oxide (GO)

Graphene-oxide was synthesized via a modified Hummers' method according to our previously reported technique.[1] Firstly, pre-oxidised graphite powder was obtained from commercially available graphite powder followed by its subsequent oxidation and exfoliation in the second step to achieve highly dispersed and well-separated graphene oxide sheets. In the initial step, Graphite powder was slowly added into concentrated H_2SO_4 solution containing P_2O_5 and $K_2S_2O_8$ kept in a hot water bath (80°C) under strong stirring for 3 h. After cooling to room temperature and diluting with Milli-Q water, a dark green mixture was obtained. The mixture was then filtered and washed several times until pH of waste solutions reaches neutral. Pre-oxidized graphite powder was collected and dried in air at room temperature overnight. In the final step, pre-oxidized graphite powder was slowly added to concentrated H_2SO_4 maintaining the temperature at 0 °C. Solid $KMnO_4$ was then added to the mixture under slow stirring and maintaining the temperature below 20 °C. After removing the ice-water bath, the mixture was heated at 35 °C under stirring for 2 h, to which Milli-Q water was then added. After a few minutes, Milli-Q water and 30% H_2O_2 solution were further added to the mixture, leading to the solution colour changed rapidly to bright yellow. The mixture was then washed with 10% HCl solution and filtered to remove residual metal ions. The raw GO suspended in Milli-Q water was centrifuged at a high rotation speed (12000 rpm). To remove residual salts and acids, the sample was further dialyzed using a dialysis tube (with a cut-off molecular weight of 12000-14000) for 7 days by regularly replacing

water bath with fresh Milli-Q water 2-3 times per day. The dialyzed GO solution was stored in a reagent bottle.

Calculations and formulas for supercapacitor performance evaluations:

The gravimetric specific capacitance (C_{SP}) can be calculated from cyclic voltammetry[2] via the equation (1)

$$C_{SP} = \frac{1}{2mv(V_f - V_i)} \int_{V_i}^{V_f} I(V)dV \qquad (1)$$

where m (in g) is the mass loading of the active electrodes in three electrode configuration, ν is the voltage scan rate, V_f and V_i (in V) are the potential limits of the CV curves, and I(V) is current at different potentials. $\int_{V_i}^{V_f} I(V)dV$ is the numerically integrated area of the CV curves.

Alternatively, the mass specific capacitance in the three-electrode configuration, C_{SP} can also be calculated from galvanostatic charge-discharge curves[2] by equation (2) as following

$$C_{SP} = \frac{I}{m}\frac{\Delta t}{\Delta V} \qquad (2)$$

where, I (in A) is the discharge current, m (in g) is the active electrode mass, Δt (in s) is the discharge time and, ΔV (in V) is the working voltage.

Similarly, the area-specific, volumetric and gravimetric specific capacitance (C_D) in the two electrode device configuration can be calculated from cyclic voltammetry *via* the equation (3)

$$C_{SP} = \frac{1}{2\langle A|V|M\rangle v(V_f - V_i)} \int_{V_i}^{V_f} I(V)dV \qquad (3)$$

where A (in cm^2) is the geometric area and V (in cm^3) is the overall volume of the device (calculated from the thickness of the device measured via cross-sectional SEM) and M (in g) is the active electrode mass in the device configuration. ν is the voltage scan rate, V_f and V_i (in V) are the potential limits of the CV curves, and I(V) is current at different potentials. $\int_{V_i}^{V_f} I(V)dV$ is the numerically integrated area of the CV curves of the electrode materials interdigitated onto the electrode surface.

Alternatively, the specific capacitance of the device, C_D can also be calculated from galvanostatic charge-discharge curves[3–6] by equation (4) as following

$$C_D = \frac{I\Delta t}{\Delta V}\frac{1}{\langle A|V|M\rangle} \qquad (4)$$

where, I (in A) is the discharge current, Δt (in s) is the discharge time, A (in cm^2) is the overall geometric area of the device, V (in cm^3) is the overall volume of the device (calculated from SEM), M (in g) is the active electrode mass and, ΔV (in V) is the working voltage.

The equations (equation 5 and equation 6) that can express the energy density (E) and power density (P) of a supercapacitor device, is given as following:

$$E = \frac{\Delta V^2}{2\times 3600}(C_D)_{\langle A|V|M\rangle} \qquad (5)$$

$$P = \frac{E\times 3600}{\Delta t} \qquad (6)$$

Where $(C_D)_A$, $(C_D)_V$ and $(C_D)_M$ is the areal, volumetric and gravimetric capacitance of the active electrodes of the binder-free all solid-state symmetric planar supercapacitor device, respectively.

Deconvolution of the cyclic voltammograms of DA-rGO and EpDA-rGO:

In order to obtain information about the charge storage kinetics of both DA-rGO and EpDA-rGO electrodes, cyclic voltammograms were recorded at various scan rates. The total stored charge can be divided into three components; (a) Non-faradaic capacitive charge storage (electrochemical double layer capacitance), (b) Faradaic non-capacitive charge storage (pseudocapacitance) and, (c) Faradaic non-capacitive charge storage (battery like behavior).[7,8] Theoretically, the current response of an active electrode material is dependent on the sweep rate via the following equation[9]:

$$i = av^b \qquad (7)$$

Where, *i* is the current, *v* is the sweep rate and *a, b* are the arbitrary coefficients. The value of '*b*' can be determined from the slope of the plot of *log i* vs *log v*. When the value of b is around 0.5, it indicates that the charge storage is controlled by semi-infinite diffusion ($i \propto \sqrt{v}$), whereas the value of b approaching 1 indicates the voltammetric response is mainly coming from the surface-confined processes; i.e., the current varies linearly with the sweep rate ($i \propto v$). Then equation 7 can be rewritten as[10],

$$i = C_d A v \qquad (8)$$

Where C_d is the capacitance and A is the electrode surface area.

In order to quantitatively determine the capacitive as well as diffusion-controlled contribution to the overall capacitance, the above equation (7) can be rewritten as[10],

$$i(V) = k_1 v + k_2 \sqrt{v} \qquad (9)$$

$$i(V)\Big/\sqrt{v} = k_1 \sqrt{v} + k_2 \qquad (10)$$

Where, *i(V)* is the measured current at the potential *V* which is comprised of both capacitive current (denoted as $k_1 v$) and diffusion-controlled current (varying with $k_2 \sqrt{v}$). Therefore, from

the slope (k_1) and intercept (k_2) of the plot of *i(V)* vs $\sqrt{v}$; it is possible to differentiate between the capacitive current and the faradaic current in the investigated rage of potentials.[11]

Calculation of surface coverage of the redox units (DA and EpDA) on the rGO matrix:

Since the charge-transfer kinetics of both DA and EpDA are mainly controlled by the surface-confined processes, therefore the surface coverage of the rGO matrix may be calculated *via* the following equation (11)

$$\tau = \frac{Q}{nFA} \qquad (11)$$

Where, Q = accumulated charge; n = number of electrons per molecule involved in the electrochemical process; F = Faraday constant and, A = electrode area.

In-plane supercapacitor device fabrication:

An all-solid-state symmetric planar supercapacitor device was fabricated using EpDA-$rGO_{1\text{-}2}$ electrode in 1 M PVA/H_2SO_4 gel electrolyte. The fabrication process of the ssd is described in detail as follows. Briefly, DA-rGO conductive ink was dropcast on 2×2 cm^2 ITO coated PET and was subjected to *in situ* polymerization to get the EpDA-rGO material. After polymerization, it was washed with DI water and then dried. After that the dried powder was collected and 20 mg of EpDA-$rGO_{1\text{-}2}$ material was dispersed in 1 mL of DMF and a conductive ink was prepared without using any binder and dropcasted again on a PET substrate to function as a binder-free solid state electrode, without the use of any current collector. The ink was spread onto a flexible PET sheet with doctor blade and dried overnight in room temperature. An in-plane supercapacitor with a linear design has been developed using a facile laser patterning process. The planar supercapacitor having finger dimensions 4

mm×0.5 mm and a finger gap of 0.15 mm was laser engraved on the EpDA-rGO/PET dried thin film. Laser patterning was achieved by using a near infra-red (NIR) laser source of 10 W. For the preparation of the gel electrolyte, typically 1 g of PVA was added to 10 mL of water and warmed to 80 °C until the solution was clear, i.e. the gel was entirely soluble in water. Stirring was continued for another 30 minutes after the addition of 1 M H_2SO_4 to prepare the solid-state gel electrolyte. Then, the gel electrolyte was spread carefully onto the laser-engraved linear in-plane design and dried to get the EpDA-rGO//EpDA-rGO symmetric all-solid-state device. The as-fabricated supercapacitor device was properly dried before testing.

Supporting Data

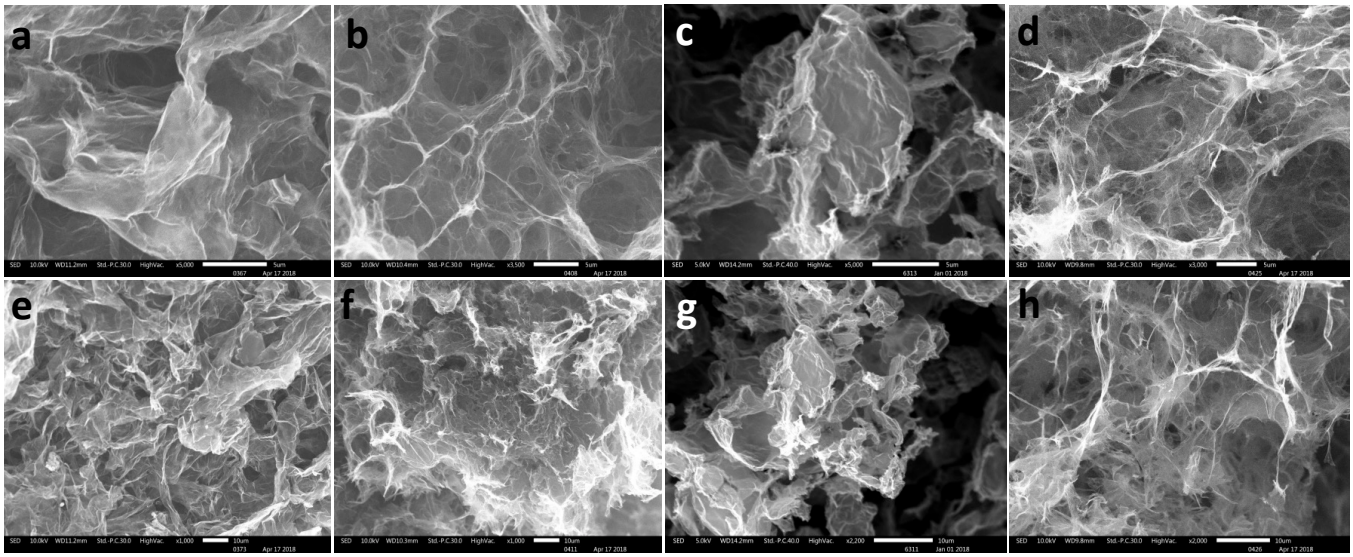

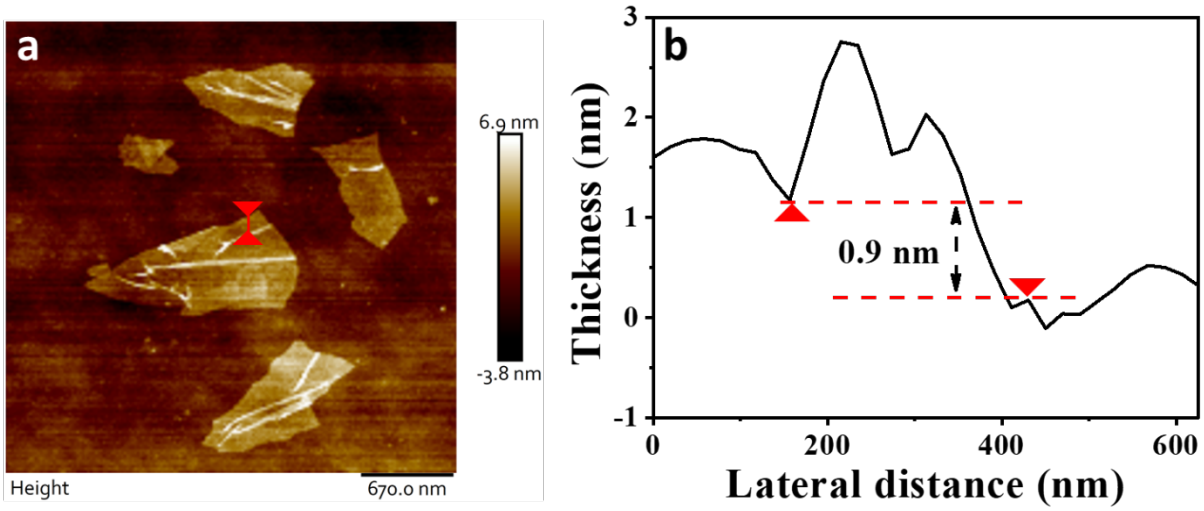

Fig. S2 (a) Surface topological analysis of GO flakes to determine its height profile, exhibited in (b), by AFM.

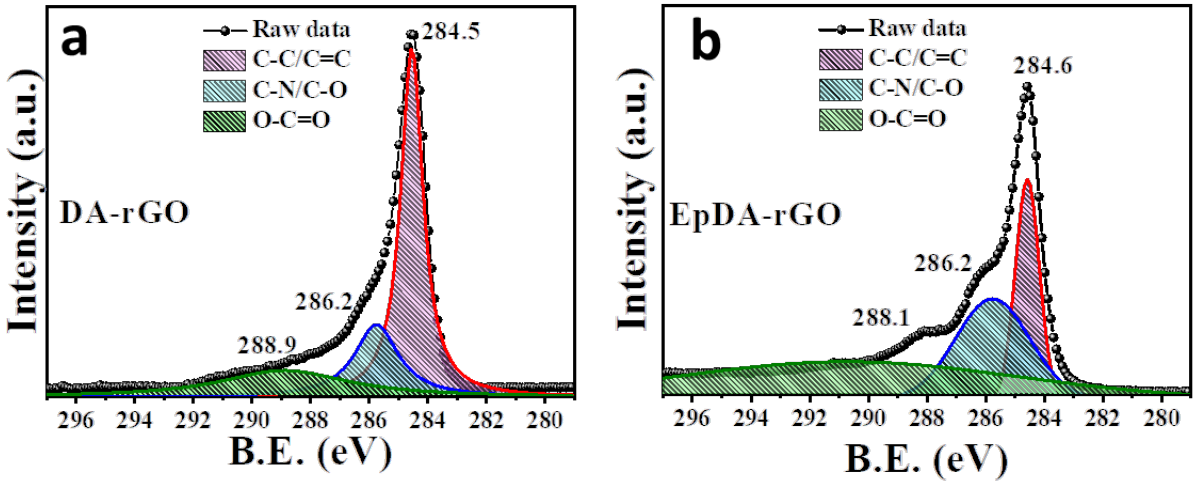

Fig. S3 High-resolution deconvoluted C1s XPS spectra (a) of the optimised xerogel material, DA-rGO and (b) the *in situ* polymerized EpDA-rGO active material.

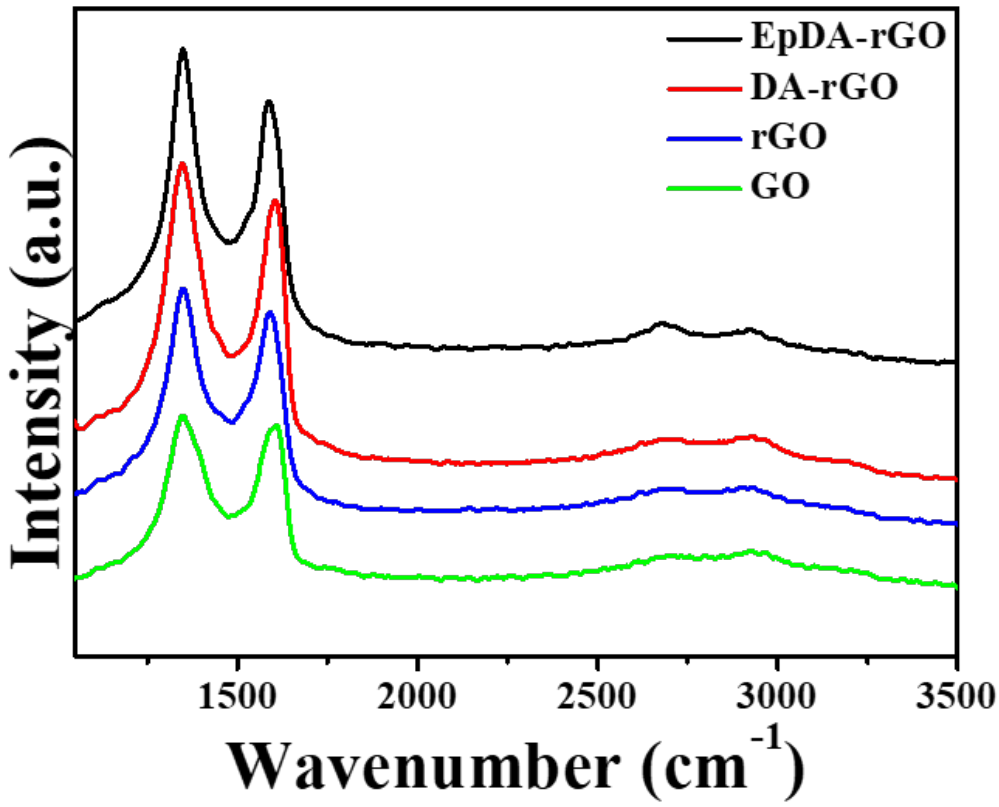

Fig. S4 Comparative Raman spectral analysis to investigate structural transformation during xerogel formation as well as *in situ* electropolymerization.

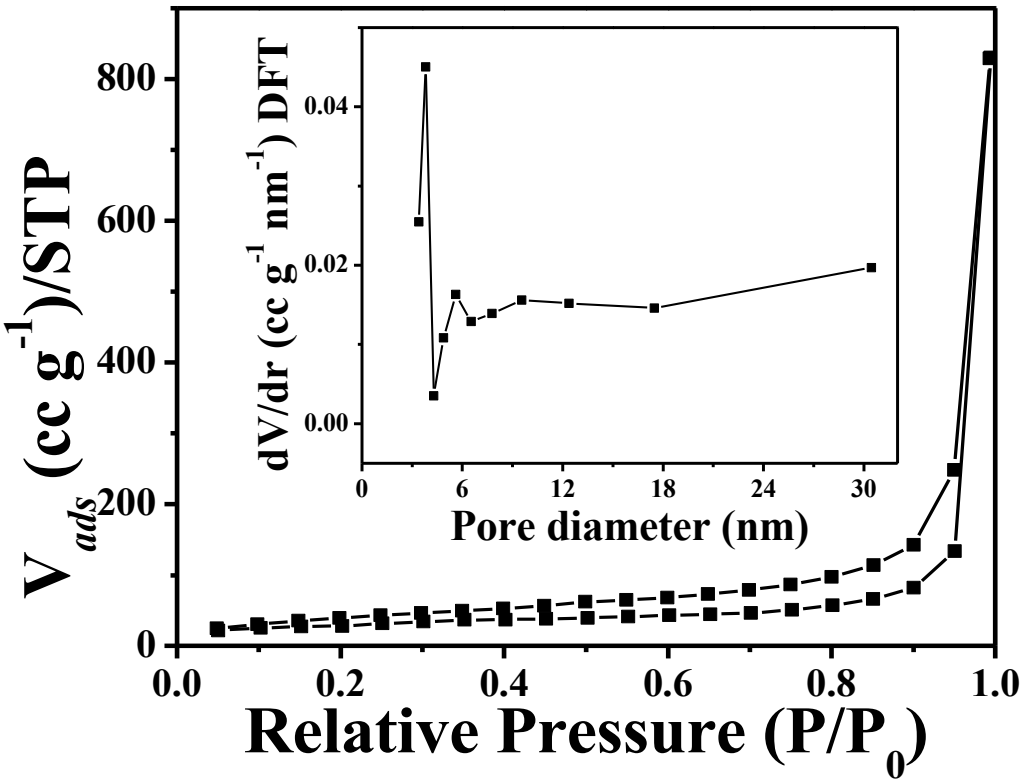

Fig. S5 N_2 adsorption desorption analysis isotherm of DA-rGO with inset showing BJH pore size distribution).

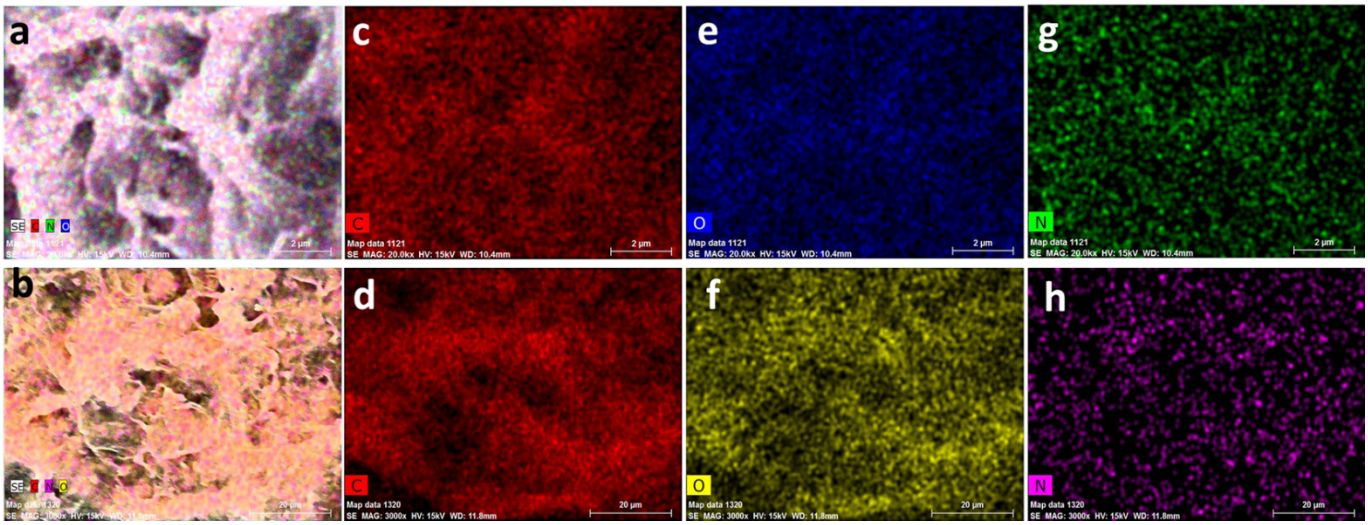

Fig. S6 Elemental mapping (a) of the xerogel structure, DA-rGO as well as (b) of the *in situ* electropolymerized EpDA-rGO showing presence of (c, d) C, (e, f) O and, (g, h) N.

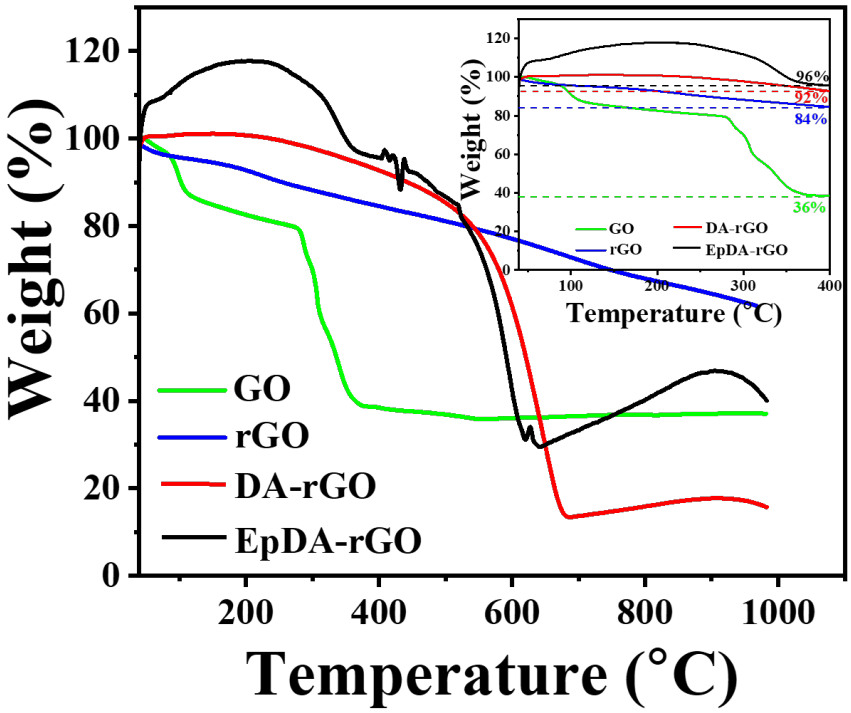

Fig. S7 Normalised TGA plots of the xerogel before and after *in situ* polymerization showing percentage weight loss with temperature as compared to GO and rGO; inset showing the mass loss in the temperature range of 40° C-400° C.

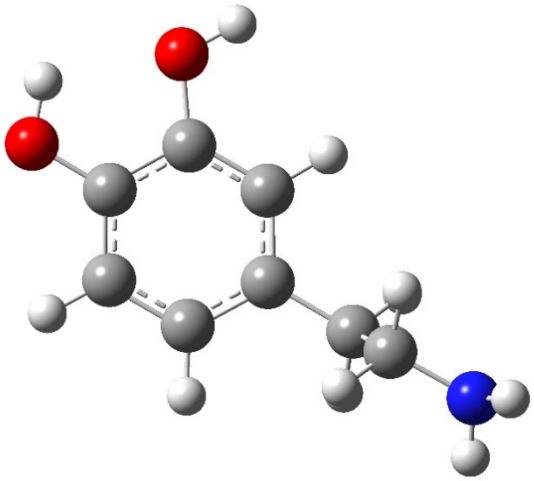

Fig. S8 Dopamine (DA) molecule, geometry optimized by using Gaussian16 package. [Gray spheres are carbon atoms, red spheres are the oxygen atoms, blue sphere is the nitrogen atom, and white spheres are hydrogen atoms]

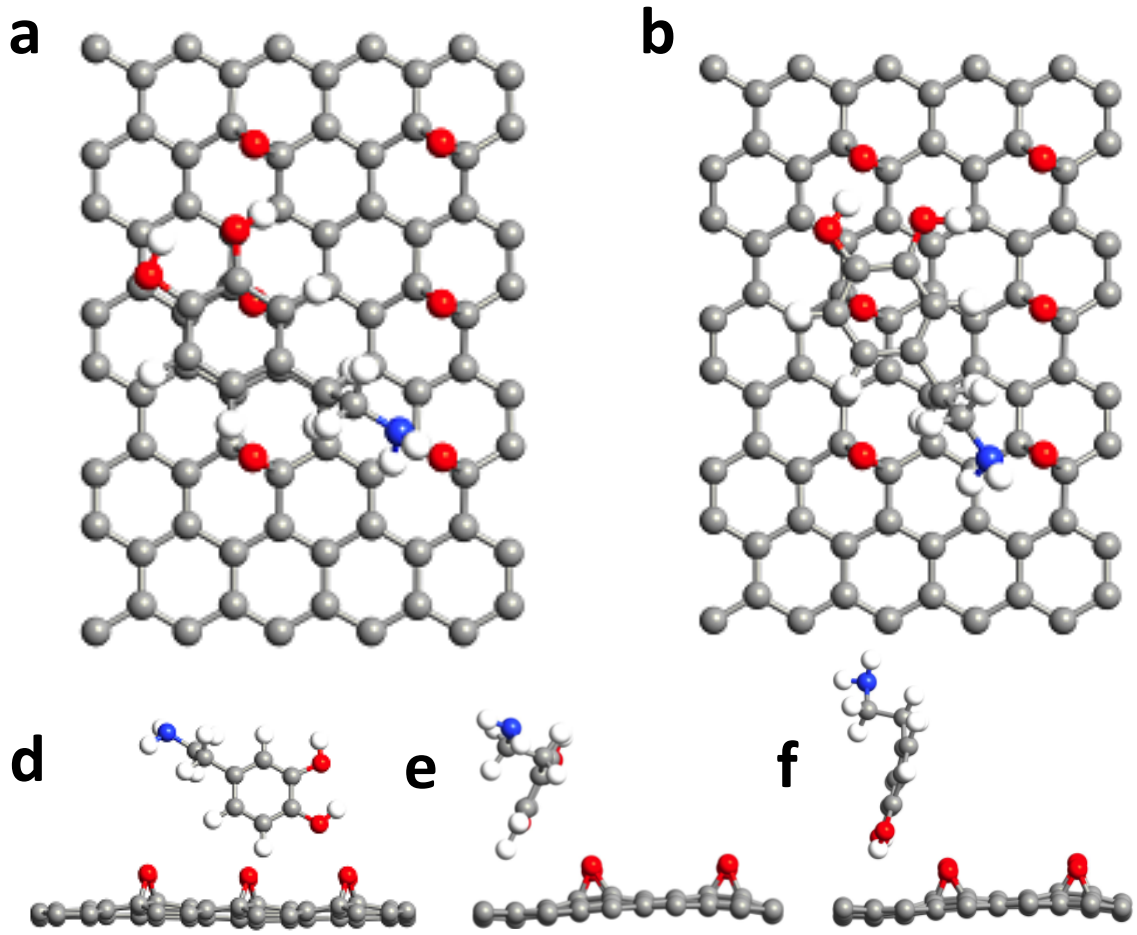

Fig. S9 Different optimized geometries of dopamine molecule aligned (a-b) parallel and (c-e) vertical, over reduced graphene-oxide sheet obtained from density functional theory (DFT) calculations.

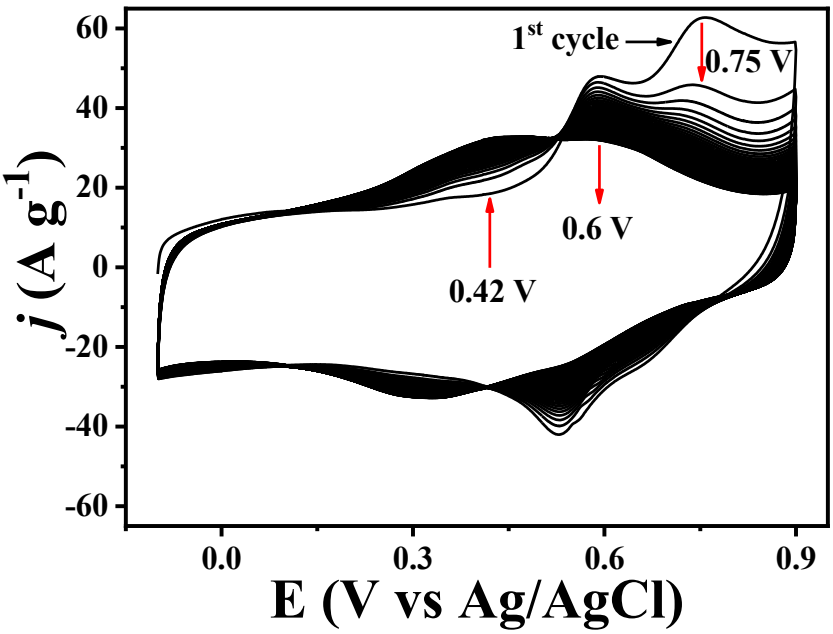

Fig. S10 Potential cycling at a scan rate of 100 mV s^{-1} showing shift in the redox peaks (marked with red arrows) corresponding to the formation of *in situ* polydopamine (EpDA) and its subsequent effect on enhancing the capacitive current as well.

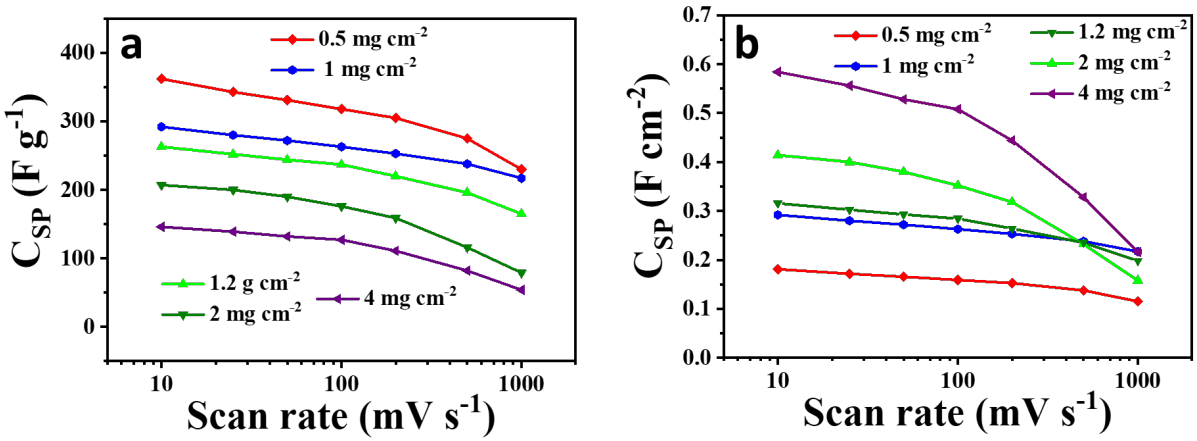

Fig. S11 Effect of mass-loading on (a) gravimetric capacitance and (b) areal capacitance at various scan rates.

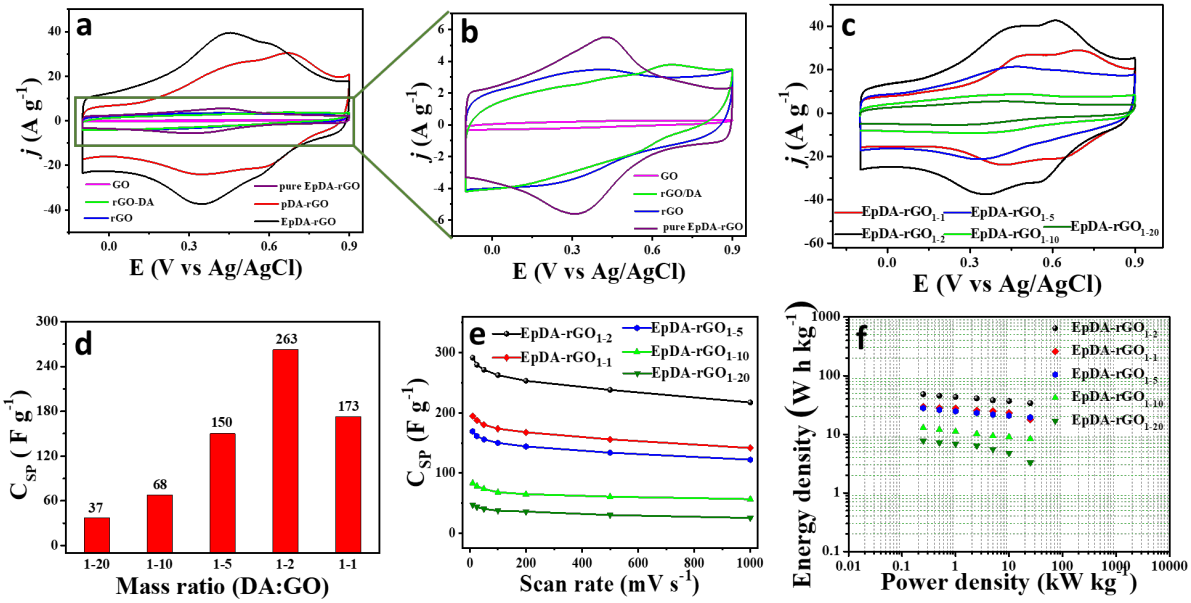

Fig. S12 (a) Comparative cyclic voltammograms of all the control electrode systems at a scan rate of 100 mV s^{-1} in an aqueous electrolyte of 1 M H_2SO_4. (b) Magnified version of Fig. S12a highlighting the CV of GO, rGO, rGO/DA and pure EpDA-rGO electrodes. Optimization of the DA mass loading on the rGO matrix, attained from electrochemical characterizations. (c) Cyclic voltammograms at a scan-rate of 100 mV s^{-1}. (d) Change in specific capacitance at a particular scan rate of 100 mV s^{-1}. (e) Effect of DA loading on the specific capacitance of various xerogel material at various scan rates. (f) Corresponding Ragone plots.

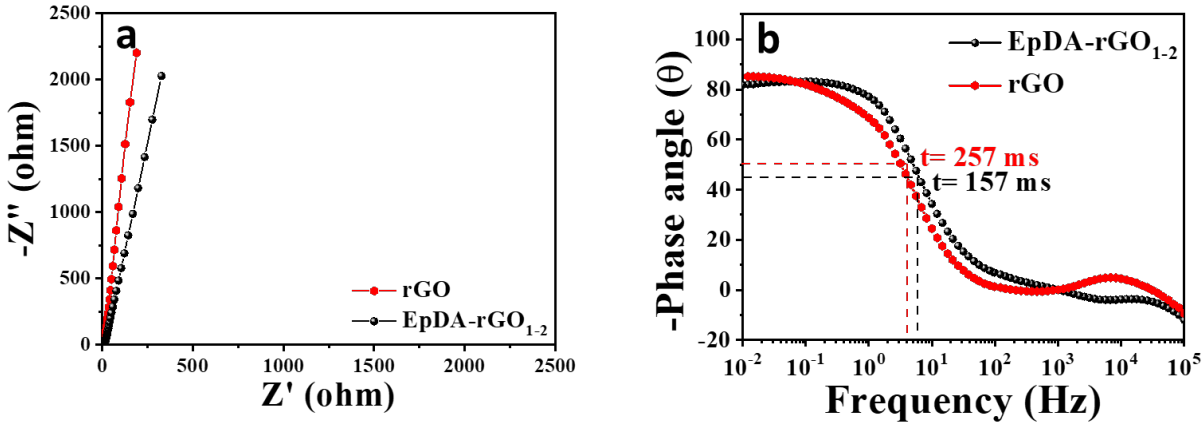

Fig. S13 (a) Comparative EIS spectra at an AC amplitude of 5 mV. (b) Corresponding Bode plots.

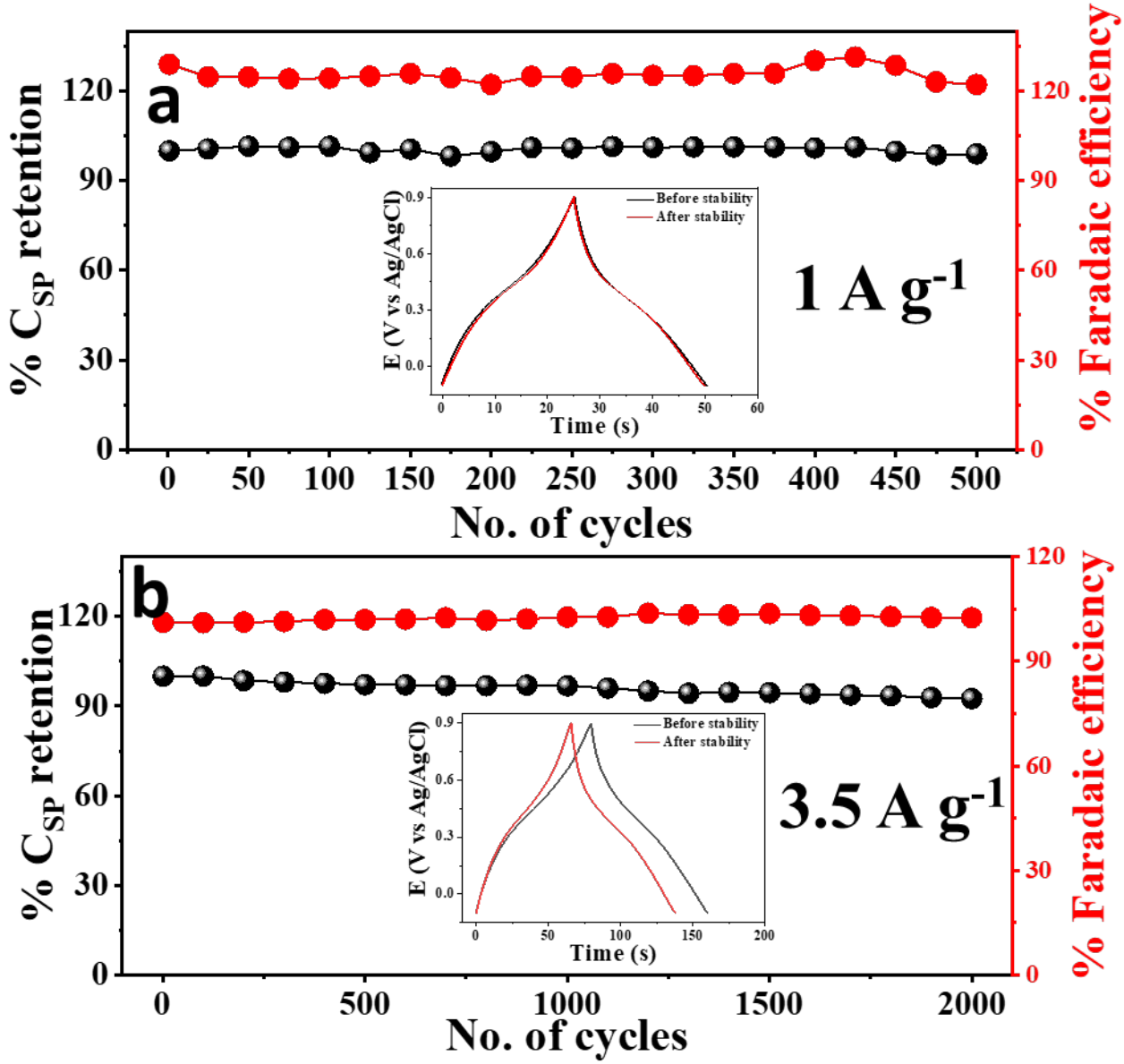

Fig. S13 Cycling stability study at various current densities for different charge-discharge time (a) 1 A g^{-1} for 500 cycles and (b) 3.5 A g^{-1} for 2000 cycles. Inset of each graph showing the before and after stability charge-discharge plots.

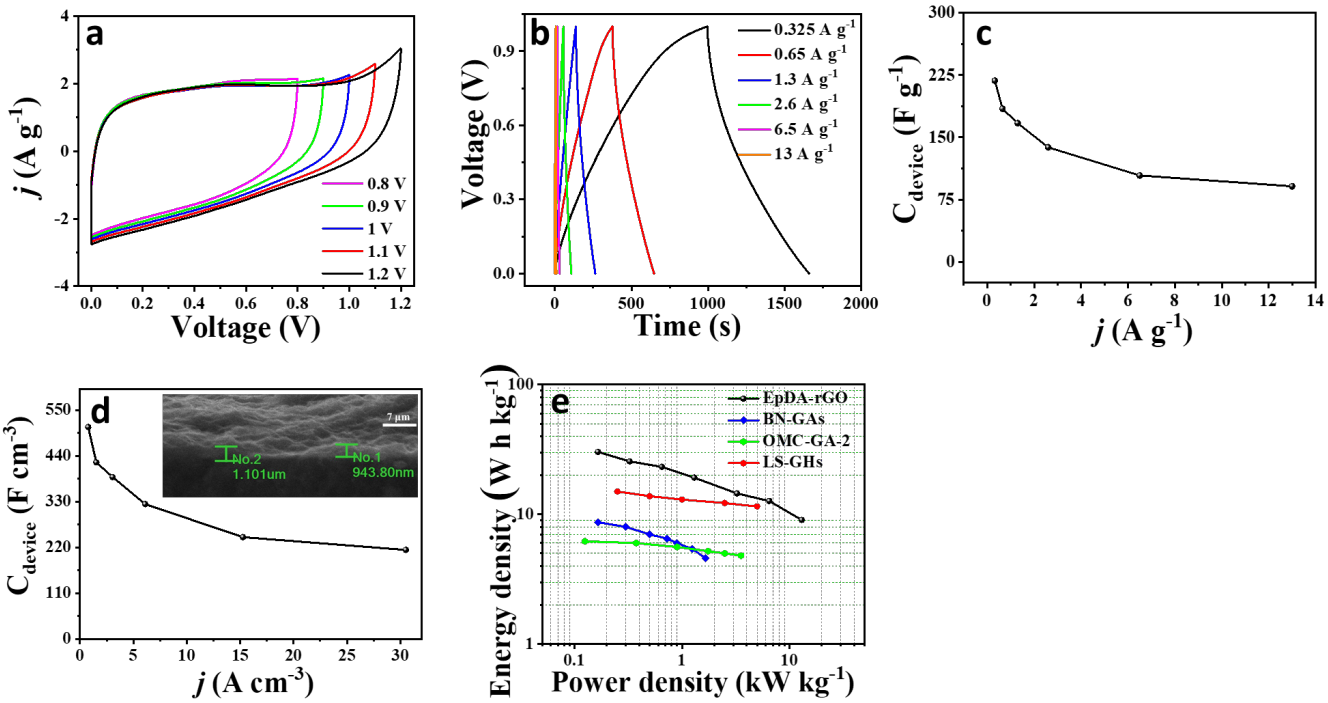

Fig. S14 (a) Optimization of the working potential window of the as-fabricated all-solid-state symmetric EpDA-rGO//EpDA-rGO device via cyclic voltammetry at a scan-rate of 10 mV s^{-1}. (b) Galvanostatic charge-discharge profiles of the device at various current densities from 0.325 to 13 A g^{-1}. (c) Rate capability in terms of gravimetric capacitance of the device with varying current density. (d) Change in volumetric capacitance of the device with varying current density; inset showing the cross-sectional SEM image of the device for measuring the thickness of the electrode materials. (e) Ragone plot of the device with some other reported literature[27,31,32] on graphene hydrogel/aerogel based solid

Table S1 Summarization of characteristic vibrational modes of DA, DA-rGO and *in situ* electrochemically oxidised pDA-rGO obtained from FTIR analysis

Vibrational Assignments	**FTIR frequencies of molecular assemblies (cm^{-1})**				**References**
	rGO	**DA**	**DA-rGO**	**EpDA-rGO**	
O-H stretching	3429	3348			12, 13
O-H/primary N-H stretching		3226	3464	3252	14
Secondary N-H stretching				3213	15
Aromatic C-H stretching	2920	3052	2930	2946	12
Aliphatic C-H stretching	2844	2954	2860		13, 16
C=O stretching	1651		1722	1712	15
Primary N-H bending		1618	1641	1647	16
N-H bending vibration of NH_3^+		1612			13
C=C ring vibration	1549	1578	1496	1452	15
C-N-C ring vibration				1368	16
N-H deformation		1281			15
C-N stretching vibration in amide			1252		14
C-N stretching in secondary amine				1152	15, 17
C-O-H deformation		1078			13
C-H in-plane bending	1095		1090	1030	15, 17
C-H out-of-plane deformation		874			12
C-H out-of-plane bending		815			12

Table S2 Comparison of key electrochemical parameters of our reported electro-active xerogel material with other contemporary organic redox centre based, conducting polymer-based as well as transition metal oxide based pseudocapacitors

Material	**Binding mode**	**Supporting electrolyte**	**Potential window**	**C_{SP} (F g^{-1})**	**Energy density (W h Kg^{-1})**	**Power density (KW Kg^{-1})**	**% Retention (Cycle number)**	**References**
Organic redox centre and graphene hydrogel based composite pseudocapacitors								
EpDA-rGO	**Covalent+ non-covalent**	**1 M H_2SO_4 (aqueous)**	**1 V (aqueous)**	**347 @ 0.5 A g^{-1} (aq)**	**48.26 (aq)**	**1000 (aq)**	**94% @ 35 A g^{-1} (53000)** **125% @ 10 A g^{-1} (20000)**	**This work**
		1 M PVA/H_2SO_4 (gel)	**1 V (gel)**	**218 @ 0.325 A g^{-1} [52 mF cm^{-2} & 509 F cm^{-3} @ 78 µA cm^{-2}] (device)**	**30.3 [70.7 W h L^{-1}] (device)**	**13.02 [30.57 W L^{-1}] (device)**	**92% @ 10 A g^{-1} (10000)**	
AZ-SGHs	Non-covalent	1 M H_2SO_4	1.4 V	350 @ 1 A g^{-1}	18.2	0.7	88% @ 5 A g^{-1} (1000)	[18]
PQ-OLC	Non-covalent	1 M H_2SO_4	0.7 V	264 @ 5 mV s^{-1}	4.5	-	97% @ 1.3 A g^{-1} (10000)	[19]
PpPD-HEG	Non-covalent	1 M H_2SO_4	1 V	248 @ 2 A g^{-1}	8.6	5	72% @ 10 A g^{-1} (1000)	[20]
DMQ@rGO	Non-covalent	1 M H_2SO_4	0.9 V	650 @ 5 mV s^{-1}	113.4	9	99% @ 50 mV s^{-1} (25000)	[21]
TBHQ@graphene	Non-covalent	1 M H_2SO_4	0.8 V	302 @ 0.25 A g^{-1}	26.84	3.2	92% @ 1 A g^{-1} (800)	[22]

AQS@rGO	Non-covalent	1 M H_2SO_4	0.7 V	567.1 @ 1 A g^{-1}	29.2	21.6	89.1% @ 10 A g^{-1} (10000)	[23]
Th-GA	Non-covalent	1 M H_2SO_4	1.4 V	384 @ 1 A g^{-1}	25.8	8.7	91% @ 10 A g^{-1} (10000)	[24]
AQ@CF	Non-covalent	1 M H_2SO_4	1.2 V	347 @ 2 A g^{-1}	19.3	72	89% @ 20 A g^{-1} (5000)	[25]
HAQ-rDCNTs	Non-covalent	1 M H_2SO_4	1 V	324 @ 1 A g^{-1}	12.3	0.7	87.5% @ 3 A g^{-1} (1000)	[26]
LS-GHs	Non-covalent	1 M PVA/ H_2SO_4	1 V	408 @ 1 A g^{-1}	13.8	5	84% @ 2 A g^{-1} (10000)	[27]
PPD-C-DCNT	Covalent	1 M H_2SO_4	1.6 V	388 @ 1 A g^{-1}	19.1	0.8	85.7% @ 5 A g^{-1} (10000)	[28]
Catechol-modified BP	Covalent	1 M H_2SO_4	1.15 V	250 @ 1 A g^{-1}	43.5	-	60% @ 7.5 A g^{-1} (10000)	[29]
ThPH-modified carbon	Covalent	1 M H_2SO_4	0.6 V	300 @ 1 A g^{-1}	15	-	69% @ 1 A g^{-1} (10000)	[30]
BN-GAs		1 M PVA/ H_2SO_4	1 V	62 @ 5 mV s^{-1}	8.7	1.65	-	[31]
OMC-GA-2		1 M PVA/ H_2SO_4	1 V	44.3@ 5 mV s^{-1}	6.2	3.545	92.6% @ 1 A g^{-1} (1000)	[32]
pDA-rGO based pseudocapacitors								
rGO/CNT-NH_2/PDA		6 M KOH	0.8 V	47.5 @ 0.1 A g^{-1} (device)	4.22	0.144	98.9% @ 2 A g^{-1} (10000)	[33]
PDA-rGO		6 M KOH	1 V	200 @ 1 A g^{-1}	-	-	99% @ 2 A g^{-1} (10000)	[34]
rGO/PDA/NF		1 M Na_2SO_4	1 V	566.9 @ 1 A g^{-1}	172.7	27.2	77.9% @ 1 A g^{-1} (1000)	[35]

rGO/PDA/ CF	1 M Na_2SO_4	0.8 V	1250 @ 2 A g^{-1}	-	-	74.5% @ 4 A g^{-1} (1000)	[36]
Other pseudocapacitive materials							
PANI-graphene foam	1 M H_2SO_4	0.8 V	491 @ 0.1 A g^{-1}	43.64	-	85% @ 5 A g^{-1} (5000)	[37]
PAG80	2 M H_2SO_4	1 V	480 @ 0.1 A g^{-1}	66.67	0.5	70% @ 1.5 A g^{-1} (400)	[38]
PVA/G/PAni-4C/G	1 M H_2SO_4	0.8 V	90 @ 3 mA	-	-	82% @ 50 mA (50000)	[39]
Ex-GF/PPy-NDS	3 M KCl	1.3 V	351 @ 1 A g^{-1}	82.4	13	82% @ 5 A g^{-1} (1000)	[40]
MnO_2/graphene	1 M Na_2SO_4	1 V	513.8 @ 1 mV s^{-1}	47.47	0.4	91.1% @ 0.4 A g^{-1} (1000)	[41]
Co_3O_4/GNS	2 M KOH	0.6 V	157.7 F g^{-1} @ 0.1 A g^{-1}	21.9	2.19	70% @ 0.2 A g^{-1} (4000)	[42]
rGO/MoO_3	1 M PVA/ H_2SO_4	1V	404 F g^{-1} @ 0.5 A g^{-1}	14	0.5	80% @ 2 A g^{-1} (5000)	[43]

EpDA- electropolymerized dopamine; rGO- reduced graphene oxide; AZ- Alizarin; -SGHs- Self-assembled graphene hydrogels; PQ- 9,10-phenanthrequinone; OLC-Onion-like carbon, PpPD - Poly (*p*-phenelyndiamine); HEG- Hydrogen exfoliated graphene; DMQ - 2,5-dimethoxy-1,4-benzoquinone; TBHQ- Tert-butylhydroquinone; AQS- Anthraquinone-2-sulfonate; Th- Thionine; GA- Graphene aerogel; AQ- Anthraquinone; HPGCFs- Hierarchically porous graphitic carbon fibres; HAQ- 1-hydroxyanthraquinone; LS-GHs Lignosulfonate functionalized graphene hydrogels; rDCNTs- Dissected carbon nanotubes with reduced graphene oxide; DA- Dopamine; PPD- p-phenylenediamine; DCNTs- Dissected carbon nanotubes; BP- Black pearl carbon; ThPH- tetrahydroxyphenazine; BN-GAs- Boron and nitrogen co-doped graphene aerogels; OMC- Ordered mesoporous carbon; CNT-NH_2- amino functionalized carbon nanotube; NF- Nickel foam; CF- Copper foam; PANI- Polyaniline; PAG80- Polyaniline-graphene (20:80); GO- Graphene oxide; PPY- Polypyrrole; PVA- Polyvinyl alcohol; G- Graphene; Ex-GF- Exfoliated graphite foil; NDS- 1,5-napthalene disulphonate; GNS- Graphene nanosheets.

References:

1 R. S. Dey, H. A. Hjuler and Q. Chi, *J. Mater. Chem. A*, 2015, **3**, 6324–6329.

2 T. Purkait, G. Singh, N. Kamboj, M. Das and R. S. Dey, *J. Mater. Chem. A*, 2018, **6**, 22858–22869.

3 P. Yang and W. Mai, *Nano Energy*, 2014, **8**, 274–290.

4 Y. Shao, M. F. El-Kady, L. J. Wang, Q. Zhang, Y. Li, H. Wang, M. F. Mousavi and R. B. Kaner, *Chem. Soc. Rev.*, 2015, 44, 3639–3665.

5 A. Ramadoss, K.-N. Kang, H.-J. Ahn, S.-I. Kim, S.-T. Ryu and J.-H. Jang, *J. Mater. Chem. A*, 2016, **4**, 4718–4727.

6 Y. Liu, B. Weng, J. M. Razal, Q. Xu, C. Zhao, Y. Hou, S. Seyedin, R. Jalili, G. G. Wallace and J. Chen, *Sci. Rep.*, 2015, **5**, 17045.

7 T. Brousse, D. Bélanger and J. W. Long, *J. Electrochem. Soc.*, 2015, **162**, A5185–A5189.

8 L. Guan, L. Yu and G. Z. Chen, *Electrochim. Acta*, 2016, **206**, 464–478.

9 V. Augustyn, J. Come, M. A. Lowe, J. W. Kim, P.-L. Taberna, S. H. Tolbert, H. D. Abruña, P. Simon and B. Dunn, *Nat. Mater.*, 2013, **12**, 518–522.

10 Y. Wang, Y. Song and Y. Xia, *Chem. Soc. Rev.*, 2016, **45**, 5925–5950.

11 C. Liu, E. I. Gillette, X. Chen, A. J. Pearse, A. C. Kozen, M. A. Schroeder, K. E. Gregorczyk, S. B. Lee and G. W. Rubloff, *Nat. Nanotechnol.*, 2014, **9**, 1031–9.

12 J. E. Carter, J. H. Johnson and D. M. Baaske, *Anal. Profiles Drug Subst. Excipients*, 1982, **11**, 257–272.

13 T. Yadav and V. Mukherjee, *J. Mol. Struct.*, 2018, **1160**, 256–270.

14 L. Q. Xu, W. J. Yang, K. G. Neoh, E. T. Kang and G. D. Fu, *Macromolecules*, 2010, **43**, 8336–8339.

15 T. Noguchi, Y. Inoue and X. S. Tang, *Biochemistry*, 1999, **38**, 399–403.

16 R. A. Zangmeister, T. A. Morris and M. J. Tarlov, *Langmuir*, 2013, **29**, 8619–8628.

17 V. Krishnakumar and R. John Xavier, *Spectrochim. Acta - Part A Mol. Biomol. Spectrosc.*, 2004, **60**, 709–714.

18 N. An, Y. An, Z. Hu, B. Guo, Y. Yang and Z. Lei, *J. Mater. Chem. A*, 2015, **3**, 22239–22246.

19 D. M. Anjos, J. K. McDonough, E. Perre, G. M. Brown, S. H. Overbury, Y. Gogotsi and V. Presser, *Nano Energy*, 2013, **2**, 702–712.

20 Jaidev and S. Ramaprabhu, *J. Mater. Chem.*, 2012, **22**, 18775–18783.

21 M. Boota, C. Chen, M. Bécuwe, L. Miao and Y. Gogotsi, *Energy Environ. Sci.*, 2016, **9**, 2586–2594.

22 H. W. Wang, H. Y. Wu, Y. Q. Chang, Y. L. Chen and Z. A. Hu, *Chinese Sci. Bull.*, 2011, **56**, 2092–2097.

23 R. Shi, C. Han, H. Duan, L. Xu, D. Zhou, H. Li, J. Li, F. Kang, B. Li and G. Wang, *Adv. Energy Mater.*, 2018, **8**, 1802088.

24 Y. Shabangoli, M. S. Rahmanifar, M. F. El-Kady, A. Noori, M. F. Mousavi and R. B. Kaner, *Adv. Energy Mater.*, 2018, **8**, 1802869.

25 H. Wang, H. Yi, C. Zhu, X. Wang and H. Jin Fan, *Nano Energy*, 2015, **13**, 658–669.

26 X. Yang, Y. Yang, Q. Zhang, X. Wang, Y. An, B. Guo, Z. Hu and H. Wu, *RSC Adv.*, 2017, **7**, 48341–48353.

27 F. Li, X. Wang and R. Sun, *J. Mater. Chem. A*, 2017, **5**, 20643–20650.

28 Y. He, X. Yang, N. An, X. Wang, Y. Yang and Z.-A. Hu, *New J. Chem.*, 2019, **43**, 1688–1698.

29 G. Pognon, C. Cougnon, D. Mayilukila and D. Bélanger, *ACS Appl. Mater. Interfaces*, 2012, **4**, 3788–3796.

30 S. Legoupy, E. Lebègue and C. Cougnon, *Electrochem. commun.*, 2016, **70**, 47–50.

31 Z. S. Wu, A. Winter, L. Chen, Y. Sun, A. Turchanin, X. Feng and K. Müllen, *Adv. Mater.*, 2012, **24**, 5130–5135.

32 R. Liu, L. Wan, S. Liu, L. Pan, D. Wu and D. Zhao, *Adv. Funct. Mater.*, 2015, **25**, 526–533.

33 Y. Xu, Y. Tao, X. Zheng, H. Ma, J. Luo, F. Kang and Q. H. Yang, *Adv. Mater.*, 2015, **27**, 8082–8087.

34 K. Zhang, L. L. Zhang, X. S. Zhao and J. Wu, *Chem. Mater.*, 2010, **22**, 1392–1401.

35 A. Khosrozadeh, G. Singh, Q. Wang, G. Luo and M. Xing, *J. Mater. Chem. A*, 2018, **6**, 21064–21077.

36 Y. Song, J. L. Xu and X. X. Liu, *J. Power Sources*, 2014, **249**, 48–58.

37 X. Feng, Z. Yan, N. Chen, Y. Zhang, Y. Ma, X. Liu, Q. Fan, L. Wang and W. Huang, *J. Mater. Chem. A*, 2013, **1**, 12818–12825.

38 Q. Guan, J. Cheng, B. Wang, W. Ni, G. Gu, X. Li, L. Huang, G. Yang and F. Nie, *ACS Appl. Mater. Interfaces*, 2014, **6**, 7626–7632.

39 X. Cao, B. Zheng, W. Shi, J. Yang, Z. Fan, Z. Luo, X. Rui, B. Chen, Q. Yan and H. Zhang, *Adv. Mater.*, 2015, **27**, 4695–4701.